Molecular beam epitaxial growth of doped oxide semiconductors

2008 J. Phys.: Condens. Matter 20 264004

(http://iopscience.iop.org/0953-8984/20/26/264004)

J. Phys.: Condens. Matter **20** (2008) 264004 (8pp) doi:10.1088/0953-8984/20/26/264004

Molecular beam epitaxial growth of doped oxide semiconductors

Scott A Chambers

Fundamental and Computational Sciences Directorate, Pacific Northwest National Laboratory, Richland, WA, USA

Received 16 October 2007
Published 9 June 2008
Online at stacks.iop.org/JPhysCM/20/264004

Abstract

Molecular beam epitaxy coupled with the use of activated oxygen is shown to be a powerful tool for the growth of well-defined, structurally excellent oxide semiconductor films. The basics of the methodology are discussed. Several case studies are presented to illustrate some of the physical phenomena that can be investigated; these include Cr- and Co-doped TiO_2 anatase, Ti-doped α-Fe_2O_3 hematite, and N-doped TiO_2 rutile.

(Some figures in this article are in colour only in the electronic version)

1. Introduction

The general topic of metal oxide thin film growth is of significant interest on a number of different scientific and technological fronts. These include next-generation gate insulators on Si, high-T_c superconductivity, ferroelectrics, multiferroics, semiconductor spintronics, chemical sensing, thermal and photocatalytic surface chemistry, and environmental surface geochemistry. The ability to generate phase-pure, structurally excellent epitaxial films of simple and complex metal oxides is of critical importance in gaining fundamental understanding of these materials in isolation, as well as in combination with one another and with other materials such as metals, elemental and compound semiconductors, and molecular adsorbates. A number of growth methods are currently employed to prepare model thin film oxides. These include reactive and nonreactive sputtering, metal organic chemical vapor deposition (MOCVD), pulsed laser deposition (PLD) and molecular beam epitaxy (MBE). Each method has certain advantages and disadvantages on issues ranging from ease of use to operating expense to time required for growth to quantity and quality of material produced. The present paper deals with MBE, specifically with the use of activated oxygen in the form of O or O_3. An important goal is to have the time for reaction between individual metal (M) and O atoms be less than the time required for metal cluster formation to occur at the growth front. The use of O or O_3, together with a sufficiently high O-to-M flux ratio, insures that this goal is met. Using O_2 can be problematic because the O_2 dissociation step is often rate limiting and sometimes thermodynamically forbidden, leading to either incomplete M oxidation or metal clusters with an oxide skin. The former can result in unintended n-type conductivity, since O vacancies are typically shallow donors in intermediate bandgap oxide semiconductors. The latter can lead to qualitatively different film morphologies and compositions.

The present paper will be limited in scope to the MBE growth and properties of doped transition metal oxide semiconductors. However, the interested reader is directed to other significant oxide MBE work focused on high-k oxide dielectrics on Si [1–9], complex oxides and high-T_c superconductivity [10–16], pure ferrimagnetic [17] and ferromagnetic [18] oxides, environmental surface geochemistry [19–24], and catalysis [25, 26].

2. Experimental details

Figure 1 shows a schematic of a flexible oxide MBE system that employs both high-temperature effusion cells and electron beam evaporators as metal sources, a quartz crystal oscillator (QCO) and atomic absorption (AA) spectrometers to monitor metal fluxes, separate atomic O and O_3 sources for activated oxygen, and reflection high-energy electron diffraction (RHEED) to monitor surface structure and morphology during growth [27].

The QCO can be positioned at the substrate position during growth in order to eliminate the need for a tooling factor correction. One of the most pressing technical issues in oxide MBE is that of metal flux variation from effusion cells upon addition of sufficiently high oxygen pressure to result in complete oxidation of the metal. Metal sublimation is an activated process, and the rate increases exponentially with temperature. A typical curve is shown in figure 2(a) for Ti.

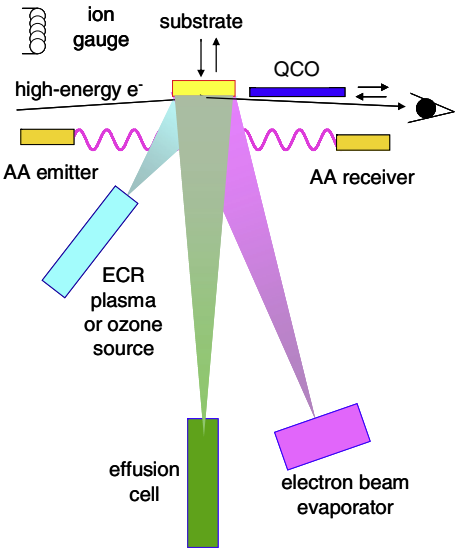

Figure 1. Schematic diagram showing elements of a functional oxide molecular beam epitaxial growth system that uses activated oxygen.

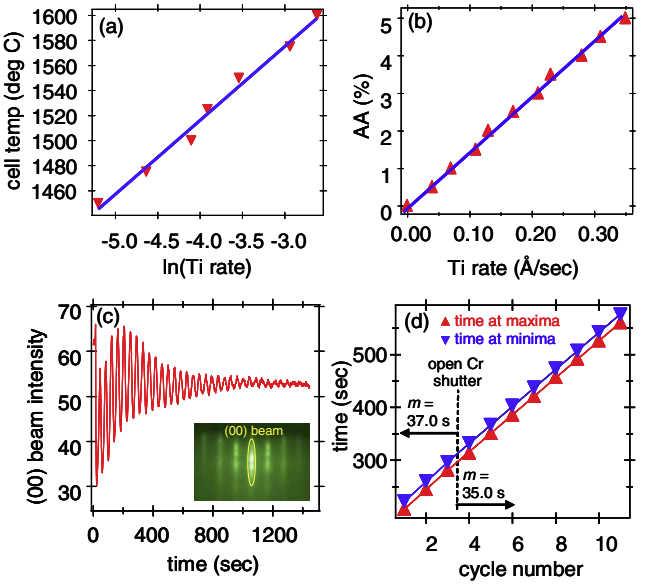

Figure 2. Essential data required to monitor metal atom beam flux and MBE growth rate: (a) deposition rate versus temperature for Ti in a high-temperature effusion cell; (b) atomic absorption versus deposition rate for Ti; (c) RHEED specular beam intensity versus time during growth of homoepitaxial N-doped TiO_2 on $TiO_2(110)$ rutile; (d) times at RHEED beam intensity maxima and minima during heteroepitaxial growth of Cr-doped TiO_2 anatase on $LaAlO_3(001)$.

The flux versus temperature calibration measured in ultrahigh vacuum changes significantly upon increasing the oxygen partial pressure in the chamber to the low 10^{-5} Torr range. The flux is typically reduced as an oxide skin forms on the surface of the hot metal charge. Therefore, the temperature versus flux data obtained in UHV are not a reliable indicator of metal deposition rate during growth. Using the QCO *during* plasma assisted MBE growth may not reliable for three reasons. First, it is not possible to position the QCO and the sample at the same location during growth, leading to potential tooling factor errors. Second, the QCO is kept near ambient temperature whereas the substrate is typically at elevated temperature and the sticking coefficient may not be the same on the two surfaces. Third, a mix of metal, suboxide and oxide species may nucleate on the QCO sensor surface, particularly if the QCO is not directly in the path of the activated O beam. This situation typically leads to a convoluted frequency response from which a unique deposition rate for the desired species cannot be unambiguously extracted. A less direct but potentially more accurate approach is to calibrate the effusion cells using activated oxygen with the QCO at the substrate position and the chamber pressure held at the growth pressure. Provided the QCO is programmed for the oxide and the metal sticking coefficient is temperature independent between ambient and growth temperature, this approach may be preferable to a UHV calibration. It will in general not work for electron beam evaporation sources due to their fast response time and lack of thermocouple.

The two other methods used for metal flux determination and oxide growth rate in our lab are atomic absorption (AA) during growth and RHEED intensity oscillations. By calibrating the element-specific AA versus evaporation rate, as seen in figure 2(b) for Ti, the AA can be used during growth to monitor the metal flux. This approach is especially valuable for electron beam evaporators. However, the limitations of AA technology in oxide MBE result from the low atom number density in the beam and the associated issue of reliable detection. For instance, we have found that the optical absorption coefficients for transition metals such as Ti, Fe and Co are sufficiently low that in combination with the low growth rates and/or at times very low atom concentrations (e.g. for dopants), it is very difficult to obtain a deposition rate that is sufficiently accurate to be useful for monitoring and control, at least with current AA technology. For example, consider Cr-doped TiO_2 anatase growth on $LaAlO_3(001)$ [28, 29]. The low growth rate required to obtain crystallographically excellent anatase ($\sim$0.015 Å s^{-1}) together with small Cr mole fraction (2–10 at.% of the cations) preclude the use of AA to monitor the Cr fluxes. In contrast, α-Cr_2O_3 heteroepitaxy on α-$Al_2O_3(0001)$ can be accurately monitored using AA because of the much higher growth rate that can be used without the film quality suffering (0.12 Å s^{-1}) [30]. In this case, the AA was successfully used not only to monitor the Cr deposition rate, but also to control the electron beam evaporator that produced the Cr beam.

Metal deposition rates are easily converted into the oxide growth rate under the assumption that the metal arrival rates are the rate limiting steps, which is true for growth under oxygen-rich conditions. RHEED intensity oscillations can be used to obtain the instantaneous oxide growth rate and, therefore, the metal evaporation rate. We show in figure 2(c) typical oscillations in the (00) beam intensity during homoepitaxial growth of N-doped TiO_2 rutile on $TiO_2(110)$ [31, 32]. The intensity maximizes upon completion of individual layers by virtue of the maximal atomic smoothness at these points in the growth. Similarly, the intensity minimizes when layers are half completed and 2D nucleation occurs randomly on terraces, giving rise to maximum atomic roughness at these points in the

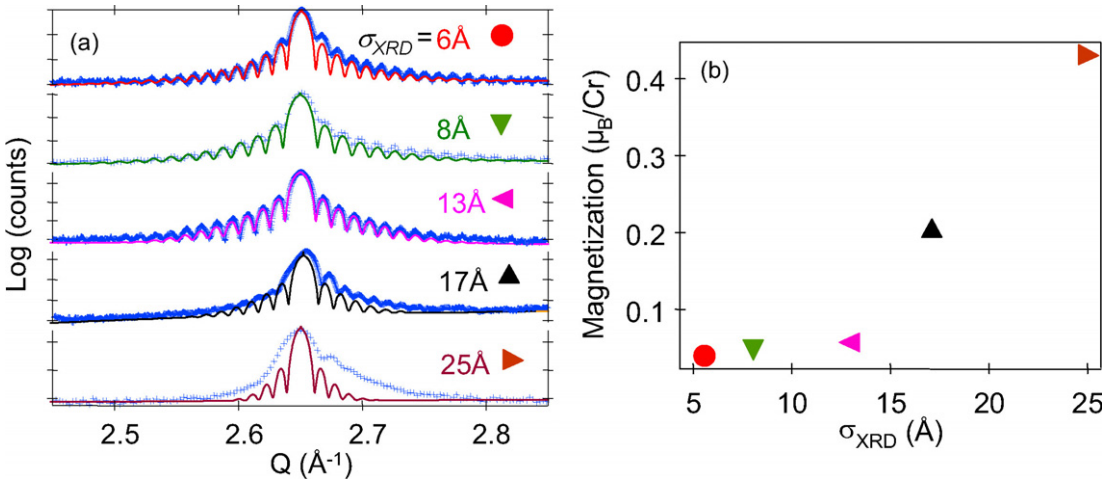

Figure 3. High-resolution XRD finite-thickness interference fringe analysis for Cr-doped TiO_2 anatase on $LaAlO_3$(001) (a), and associated room temperature, in-plane saturation magnetic moment data (b). Reprinted figure with permission from [29]. Copyright 2006 by the American Physical Society.

growth. The oscillations often decay in amplitude as growth proceeds, as seen in figure 2(c). This phenomenon typically occurs because the film surface roughens and 2D layer-by-layer growth ceases due to strain relief, a substrate temperature that is either too high or too low, and/or deviations from ideal stoichiometry in the case of complex oxides. The RHEED streaks develop modulated intensities as roughness sets in, as seen in the inset to figure 2(c). In the case of metal-doped metal oxides grown under oxygen-rich conditions, the RHEED period will be different for the doped oxide compared to the pure oxide, as illustrated in figure 2(d) for Cr-doped TiO_2 anatase grown on $LaAlO_3$(001) [33]. Here we plot the time at intensity maxima and minima versus cycle number, starting with the growth of a pure TiO_2 layer for three cycles, and then abruptly transitioning to Cr-doped TiO_2 growth. The Ti flux was not changed when the Cr shutter was opened. The Ti-to-Cr atom flux ratio was ∼9:1, so an ∼10% increase in growth rate is expected upon opening the Cr shutter. A ∼5% (rather than 10%) reduction in period actually occurs when the Cr shutter is opened. Since Cr occupies cation sites in the anatase lattice, the formation of layers is accelerated by ∼5%, giving rise to a faster overall growth rate. The factor-of-two discrepancy between the RHEED oscillation period change and the estimated total metal atom flux change associated with opening the Cr shutter is a result of the oxide skin effect, as described above.

3. Case studies

3.1. Cr-doped TiO_2 anatase

Metal oxides doped with a few to several atomic per cent of some transition metal with unpaired d electrons have been of considerable interest in the magnetic materials and semiconductor communities since the publication of initial theoretical [34] and experimental [35] studies. These studies theoretically predicted and generated experimental evidence for ferromagnetism at ambient temperature in Mn-doped ZnO and Co-doped TiO_2 anatase, respectively. Yet, despite considerable effort on these and other alleged high-T_c ferromagnetic semiconductors, the initial results have been moderately to notoriously difficult to reproduce, and the mechanism(s) of magnetism remains elusive [36]. In some cases, the formation of ferromagnetic secondary phases resulting from exceeding the solid solubility of the dopant in the host matrix has resulted in spurious magnetic properties. In the ideal material, gateable free carriers would align the dopant spins in a controllable way, giving rise to a spin polarized majority band current at and above room temperature. However, this outcome has not been unambiguously demonstrated. A major problem in the field is that of material quality. Many groups have based their conclusions on material of dubious structural and/or compositional homogeneity and quality. In general, the heteroepitaxy has not been optimized, nor have the resulting materials been adequately characterized, resulting in a lack of insight into the true mechanism(s) of ferromagnetism.

Cr-doped TiO_2 anatase grown on $LaAlO_3$(001) and $SrTiO_3$(001) constitutes a good example of one such material. Early MBE growth demonstrated unambiguously that Cr(III) substitutes for Ti(IV) in the lattice with a nearly random spatial distribution, and that this material is ferromagnetic at and above room temperature [33, 37]. The films could be made n-type by post-growth annealing to create O vacancies. However, the films did not exhibit an anomalous Hall effect, indicating that there was no interaction between the free carriers and the Cr dopant spins. Moreover, the films were not of particularly good crystallographic quality. Although the material was (001)-oriented anatase, the mosaic spread was high and the film surfaces were rather rough. In order to determine the relationship between overall crystallographic quality and microstructure on the one hand, and magnetic and electrical transport properties on the other, Kaspar *et al* [28, 29] determined a set of growth conditions that gave rise to films with vastly superior crystallographic and morphologic quality compared to what had been grown before. The growth rate was very slow (∼0.015 Å s^{-1}). The resulting films exhibited very narrow rocking curve widths and low

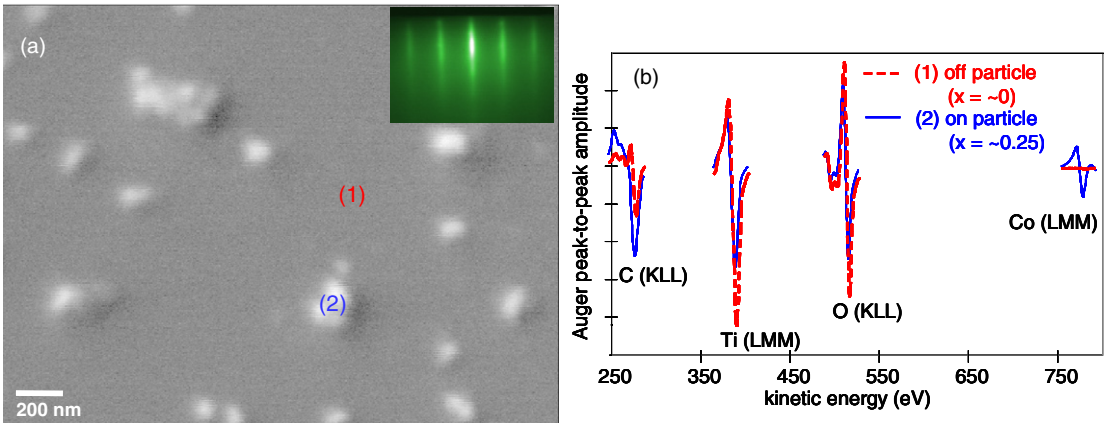

Figure 4. Scanning Auger microprobe secondary electron image for epitaxial Co-doped TiO_2 anatase on $LaAlO_3(001)$ (a), and point Auger spectra on and off surface particles (b).

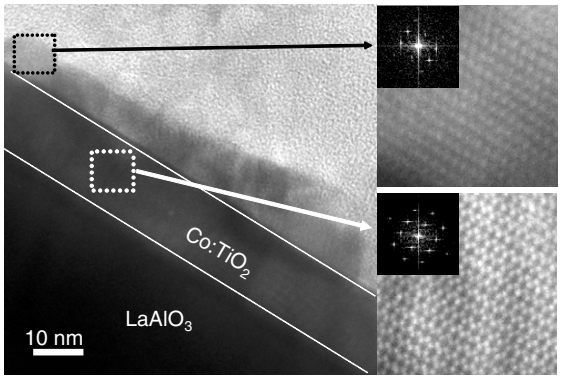

Figure 5. TEM cross sectional image of a surface particle of Co-enriched $Co_xTi_{1-x}O_2$ anatase embedded in a continuous epitaxial film of $Co_xTi_{1-x}O_2$ anatase grown on $LaAlO_3(001)$. Reprinted with permission from [44]. Copyright 2003, American Institute of Physics.

mosaic spreads. Furthermore, a systematic anticorrelation was found between crystallographic quality and room temperature saturation magnetic moment. We show in figure 3(a) fits of the anatase (004) Bragg reflection and the associated finite-thickness interference fringes to a simple model for Cr:TiO_2 films of various extents of structural quality.

The model takes into account the interference of wave fields scattered by atomic planes over the finite thickness of the film. These oscillations can be modeled as

$$I(Q) = \frac{\sin^2(QL/2)}{\sin^2(Qd/2)} \exp(-|Q - 2\pi/d|\sigma_{\mathrm{XRD}}) \qquad (1)$$

where $I(Q)$ is the scattered x-ray intensity, Q is the scattering vector given by $Q = (4\pi/\lambda)\sin\theta$ where λ is the x-ray wavelength and θ is the angle of x-ray incidence with respect to the surface and interface planes, d is the anatase layer spacing along the (001) direction, and σ_{XRD} is an overall measure of the film structural quality and roughness. The scans are plotted in order of increasing σ_{XRD}. The fringes begin to damp out in the bottom two scans as a result of multiple and overlapping Bragg peaks associated with increasing mosaic spread. In figure 3(b) the dependence of the room temperature in-plane saturation magnetization on σ_{XRD} is shown. The observed anticorrelation between magnetization and crystal quality suggests that defects associated with poor crystallinity activate the magnetic ordering. This conclusion is at least qualitatively consistent with the donor impurity band exchange model developed by Coey *et al* [38]. In this material, the active defect that gives rise to a spin-split impurity band would be something like O vacancies (O_v) at small-angle grain boundaries associated with high mosaic spread, rather than charge-compensating O_v associated with substitutional Cr(III) at Ti(IV) lattice sites. The latter defect should be present in all Cr:TiO_2 films, independent of crystallographic quality. Interestingly, Ye and Freeman [39] have predicted with all-electron first principles calculations that substitutional Cr(III) dopants compensated by O_v do *not* couple to a ferromagnetic ground state, whereas uncompensated substitutional Cr(VI) dopants do. However, the lattice apparently does not stabilize substitutional Cr(IV). The implication of O_v defects at small-angle grain boundaries is consistent with the properties of Cr- and Co-doped anatase nanoparticles and nanorods which are paramagnetic as grown, but which develop room temperature ferromagnetism when annealed in air as either agglomerated nanoparticles or films spin coated onto polycrystalline sapphire substrates [40, 41].

3.2. *Co-doped TiO_2 anatase*

MBE-grown Co-doped anatase behaves qualitatively differently than Cr-doped anatase. The Co dopants tend to segregate into regions of Co-enriched $Co_xTi_{1-x}O_2$ anatase in which all Co is substitutional Co(II), yet x is considerably larger than that expected from the fluxes [42–44]. This unusual phase consists of low-aspect-ratio Co-rich $Co_xTi_{1-x}O_2$ anatase epitaxial particles that sit atop a continuous epitaxial $Co_xTi_{1-x}O_2$ anatase film in which x is much lower than expected from the fluxes, as seen in figures 4 and 5.

The SEM image (figure 4(a)) clearly shows the presence of surface particles. The associated RHEED pattern (inset in figure 4(a)) reveals that the particles do not result in either

polycrystalline rings or additional spots, implying that the particles consist of anatase in the same orientation as the underlying film. However, the Auger point spectra (figure 4(b)) obtained on and off the particles reveal a large difference in Co concentration. The cross sectional TEM image (figure 5) shows one particle atop the continuous film, and the selected area diffraction patterns reveal that both are anatase with the orientation based on the expected epitaxial relationship—$(001)_{ana} \parallel (001)_{LAO}$ and $[100]_{ana} \parallel [100]_{LAO}$. In other words, the Co-rich $Co_xTi_{1-x}O_2$ particles nucleate directly on the Co-poor $Co_xTi_{1-x}O_2$ continuous film.

Co-doped anatase is insulating as grown under oxygen-rich conditions, but can be made n-type by reducing the oxygen pressure during growth, or by post-growth annealing in high vacuum. This material exhibits room temperature ferromagnetism in either the insulating or semiconducting state, as well as an anomalous Hall effect [45] and very weak Co L-edge x-ray magnetic circular dichroism [46], both at room temperature, when n-type. Therefore, in a limited sense, Co-doped anatase bears the marks of a magnetic semiconductor, although the unusual nonhomogeneous composition precludes use of the adjective 'dilute'. There is apparently a magnetic interaction between free carriers in the anatase semiconductor and magnetic entities within the film, as judged by the observation of an anomalous Hall effect. It must be emphasized that these magnetic entities are *not* Co metal clusters, but rather mesoscale high-x $Co_xTi_{1-x}O_2$ anatase particles that exhibit perpendicular domain walls in magnetic force microscopy [44]. These particles have no counterpart in the bulk, but rather are stabilized within a low-$x$$Co_xTi_{1-x}O_2$ matrix during MBE growth. The close proximity of Co(II) dopants in the Co-rich $Co_xTi_{1-x}O_2$ phase, together with electrons from charge-compensating O_v defects, presumably give rise to the ferromagnetic state in the absence of free carriers.

3.3. Ti-doped Fe_2O_3 hematite

As an alternative approach to doping diamagnetic semiconductors with magnetic cations, we consider doping an antiferromagnetic charge-transfer insulator containing cation layers in which the collective spin orientation alternates from layer to layer with a nonmagnetic cation (e.g. one with no unpaired d electrons). The idea is to see if selective replacement of magnetic ions occurs preferentially in one magnetic sublattice, leading to a net spin, as theoretically predicted by Butler *et al* [47]. We have carried out this experiment using α-$Fe_2O_3(0001)$ (hematite) as the host lattice and Ti as the dopant [48]. Hematite is a canted antiferromagnetic oxide with high-spin Fe(III) bilayers of opposite spin orientation separated by a close-packed O^{2-} layer along the c axis. The magnetic structure along the c axis can be represented as O_3–M_α–M_α–O_3–M_β–M_β–O_3–M_α–M_α–O_3–M_β–M_β–O_3-$\cdots$, where α and β denote spin up and spin down, respectively. Ti(IV) is a d^0 cation, and if it substitutes for Fe(III) preferentially in either the spin-up or spin-down magnetic sublattice as predicted, the material will develop a net spin with a saturation moment proportional to the Ti concentration. Conversely, if Ti(IV) dopants replace Fe(III) ions randomly in both magnetic sublattices, the net spin should remain approximately zero. Butler *et al* [47] have predicted that Ti substitutes preferentially for Fe(III) cations in alternating cation bilayers, resulting in a ferrimagnetic semiconductor with an effective net magnetic moment of $4\mu_B$/Ti atom. Adding Coulomb repulsion to the local spin-density approximation (LSDA + U) predicted insulating behavior with Ti donor electrons being localized on a neighboring Fe site, effectively reducing these irons from +3 to +2 formal charge states.

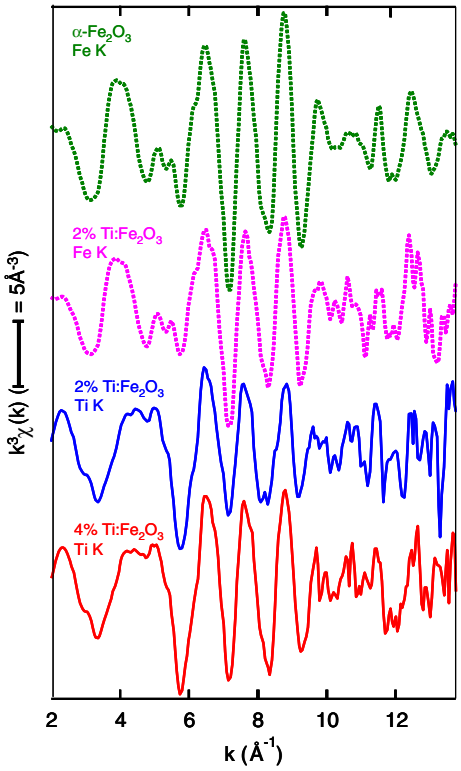

Figure 6. Fe (dashed) and Ti (solid) K-shell EXAFS from epitaxial α-$Ti_xFe_{2-x}O_3/\alpha$-Cr_2O_3/α-$Al_2O_3(0001)$ for $x = 0$, 0.02 and 0.04. Reprinted figure with permission from [48]. Copyright 2007 by the American Physical Society.

We have grown α-$Ti_xFe_{2-x}O_3(0001)$ on α-$Al_2O_3(0001)$, using a ~100 Å thick layer of α-$Cr_2O_3(0001)$ as a buffer layer to grade the lattice mismatch [30, 48]. Ti K-shell XANES (not shown) reveals that Ti is present as Ti(IV) for x up to at least 0.08, the highest concentration measured with this spectroscopy. Ti K-shell EXAFS indicates that Ti(VI) substitutes for Fe(III) for x up to at least 0.04, the highest concentration measured by EXAFS. These data are shown in figure 6.

Not only is there an excellent match between the Ti K-shell EXAFS for the doped films with those associated with the Fe K shell in both pure and Ti-doped Fe_2O_3, but EXAFS modeling shows conclusively that Ti occupies Fe sites in the corundum lattice. Substitutional Ti(IV) might be expected to be an ionized donor in α-Fe_2O_3. However, while the conductivity increases modestly with increasing x, it never reaches the level expected for a highly doped n-type semiconductor. At the same time, Fe 2p core-level and valence

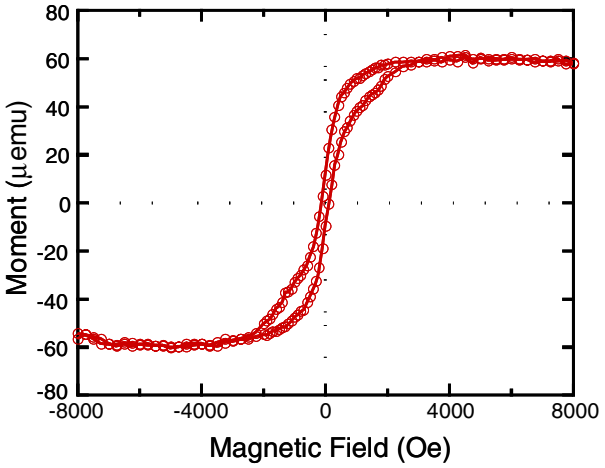

Figure 7. In-plane vibrating sample magnetometry loop measured at room temperature for epitaxial α-$Ti_{0.08}Fe_{0.92}O_3/\alpha$-$Cr_2O_3/\alpha$-$Al_2O_3(0001)$. Reprinted figure with permission from [48]. Copyright 2007 by the American Physical Society.

band photoemission spectra (not shown) clearly reveal features associated with Fe(II) at $x = 0.15$. Taken together, these data suggest that donor electrons from Ti(IV) become localized on Fe sites, converted a measurable fraction to Fe(II) at higher x. The magnetization loops, as seen for a typical film in figure 7, exhibit an interesting dual-lobe structure for all x, suggestive of two magnetic phases with high and low coercivities.

The saturation moment averaged over all values of x investigated is 0.5 ± 0.2 μ_B per Ti. This value is lower than expected if the Ti dopants exclusively occupy sites in one particular magnetic sublattice, but is clearly nonzero. These results are best interpreted as being due to partial nucleation of the nonrandom dopant phase. That is, some regions of the film volume consist of the antiferromagnetic random solid solution. In other regions, the Ti ions preferentially substitute in one particular sublattice, giving rise to ferrimagnetic behavior. The high-coercivity portion of the ferromagnetic phase may contain antiphase boundaries that are harder to switch due to grain boundary domain wall pinning. Further testing of this hypothesis requires higher-resolution STEM and spatially resolved EELS, and such measurements are in progress.

Based on a saturation moment of $\sim$0.5 μ_B per Ti, we estimate that $\sim 1/8$ of the Ti is in regions characterized by a nonrandom, magnetic-sublattice-specific configuration. This conclusion is consistent with our *ab initio* DFT/Hartree–Fock hybrid functional calculations, which correctly predict pure hematite to be a charge-transfer insulator for which the bottom of the conduction band is dominated by Fe 3d states [48]. These calculations also predict Ti–O bond lengths in $Ti_xFe_{2-x}O_3$ that are in excellent agreement with EXAFS experiment. Significantly, these calculations predict an energy difference of only 0.038 eV per supercell between the random solid solution and the magnetic-sublattice-specific configuration. The interpretation of our experimental results based on coexistence of two magnetic phases is thus underpinned by theory. We are currently working on elucidating the microstructure of the magnetic-sublattice-specific configuration by high-resolution STEM.

3.4. N-doped TiO_2 rutile and anatase

Anion doping of TM oxides is also of interest, but for a very different set of scientific reasons. Anion dopants are expected to be acceptors in TM oxides, and p-type doping is essential to making lasers and light emitting diodes from light emitting oxide semiconductors such as ZnO. The prospect of reducing the host oxide bandgap to enhance visible light absorption, electron–hole pair creation and enhanced photochemical activity at wavelengths for which the solar spectrum is rich has also motivated anion doping, particularly for TiO_2. Photochemical processes of interest include organic molecule destruction and water splitting for H_2 production. Anion doping appears to be useful for bandgap reduction. Recent studies have reported an enhancement of visible light photocatalytic activity in anion-doped TiO_2 powders [49]. In order to gain deeper fundamental understanding of this material, several groups have attempted to prepare model films and surfaces. Methods include magnetron sputtering [49–51], ion implantation [52] and pulsed laser deposition [53–55]. A drawback common to these approaches is that unintended defects are introduced by growth and implantation processes. Such defects mask the fundamental interactions of the dopant with the lattice by introducing additional defect–dopant–lattice interactions. Better controlled specimen preparation and more thorough characterization are essential in elucidating dopant–lattice interactions in a definitive way.

MBE constitutes an ideal way to grow this material. N_2 and O_2 can be mixed in the ECR plasma tube (figure 1) to generate a mixed beam of N and O radicals. Alternatively, the ECR plasma can be used to generate N and the ozone source for O. Both approaches have been used in our laboratory, and generate essentially identical results. We have grown both anatase and rutile $TiO_{2-x}N_x$ films. Rutile was grown on $TiO_2(110)$ and α-$Al_2O_3(0001)$ substrates [31, 32], and anatase was grown on $LaAlO_3(001)$ substrates [56]. N substitutes for O in both lattices and exhibits a -3 formal charge state. N incorporation appears to be limited to less than $\sim$2 at.% of the anions in rutile, and $\sim$0.2% in anatase in materials grown under optimized conditions. Interestingly, N acceptors are fully compensated by Ti interstitials that form during MBE growth, precluding p-type behavior. N incorporation results in substantial bandgap reduction due to N 2p-derived states that form at the top of the valence band. However, we do not yet know if holes generated by photoexcitation from these states will be mobile and photochemically active at the surface, or remain localized on their respective N sites.

Deviation from optimized conditions rapidly leads to crystallographically poor material and, in some cases, secondary phase formation. These results are illustrated in figure 8 and 9, where RHEED and core-level XPS area shown for three $TiO_{2-x}N_x$ rutile films grown on $TiO_2(110)$. Conditions set A (the optimized set) consists of a Ti atom flux of 0.038 Å s^{-1}, and O_2 and N_2 MBE chamber partial pressures of 4.0×10^{-6} Torr for each gas. In condition set B, the Ti atom flux was doubled (relative to A), and the O_2 and N_2 partial pressures were unchanged. Condition set C is the same as B, except that the N_2 partial pressure is zero. In all cases, the O to Ti atom flux ratio is at least an order of

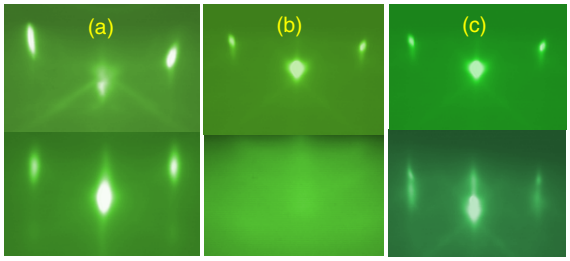

Figure 8. RHEED patterns for various $N_xTi_{1-x}O_2$ rutile films grown on rutile $TiO_2(110)$. In (a) the Ti atom flux was 0.038 Å s^{-1}, and the O_2 and N_2 partial pressures were both 4.0×10^{-6} Torr. In (b) the N_2 and O_2 partial pressures were the same as in (a), but the Ti flux was doubled. In (c), the Ti flux and O_2 partial pressure were the same as in (b), but no N_2 was admitted into the chamber. The top and bottom rows are for the substrates and films, respectively.

magnitude greater than unity, insuring that there is adequate O present to fully oxidize all incoming Ti, provided no secondary phase formation occurs. As seen in figure 8, the RHEED patterns for the films (lower row) are essentially the same as those of the associated substrates (upper row) for condition sets A and C, indicating excellent homoepitaxy. However, film B is disordered (lower middle RHEED pattern in figure 8). Likewise, as seen in figure 9, left panel, the lattice N peak in the N 1s spectrum for film B is shifted ∼0.4 eV to higher binding energy relative to film A, indicating a different N specification. The Ti $2p_{3/2}$ spectrum for film A consists of the primary lattice peak at 458.9 eV and a weaker feature that can be fit to a similar line shape ∼1 eV to lower binding energy (inset to figure 9, right panel). Based on statistical analysis and correlation with the N 1s intensities, these two peaks are assigned to Ti in the coordination environments Ti–O_6 and Ti–$O_{5-\delta}N_{1+\delta}$, respectively. However, the spectrum for film B shows substantial broadening as well as peaks at the Ti(III) binding energies for each spin–orbit channel (∼463 and ∼457 eV). That the Ti(III) present in film B is *not* due to inadequate oxygen flux at the growth front is discerned by noting that the spectrum for film C consists of sharp singlets at the binding energies of Ti(IV). Taken together, these results indicate that disordered secondary phase formation occurs as a result of deviation form the ideal, optimized fluxes. Indeed, glancing incidence XRD (not shown) reveals the presence of weak Bragg reflections for Ti_2N and $TiO_{1.2}$.

The results for N-doped anatase are largely the same as those for N-doped rutile, with one important exception. The solubility of N in well-defined epitaxial anatase is ∼10x lower than that in rutile. Therefore, the maximum x is ∼0.002 in structurally well-defined $TiO_{2-x}N_x$ anatase epitaxial films. However, as in the case of N-doped rutile, it is possible to achieve an *apparently* higher value of x by decreasing the O-to-Ti flux ratio while remaining in the anion-rich regime. Doing so leads to significant quantities of Ti(III) in the near-surface region, a condition that disappears if the N beam is turned off [56]. Therefore, the formation of secondary N-containing phases that include reduced Ti appears to be the best explanation for these results, and the apparent increase in x is spurious.

4. Summary

The use of MBE to prepare well-defined oxide semiconductors has resulted in a number of scientifically illuminating investigations to date. The level of process control afforded by the use of MBE is in principle unprecedented, but in practice is limited by a number of factors. Future advances in the field will require technological progress, primarily in the areas of accurate flux monitoring and control at very low values, and

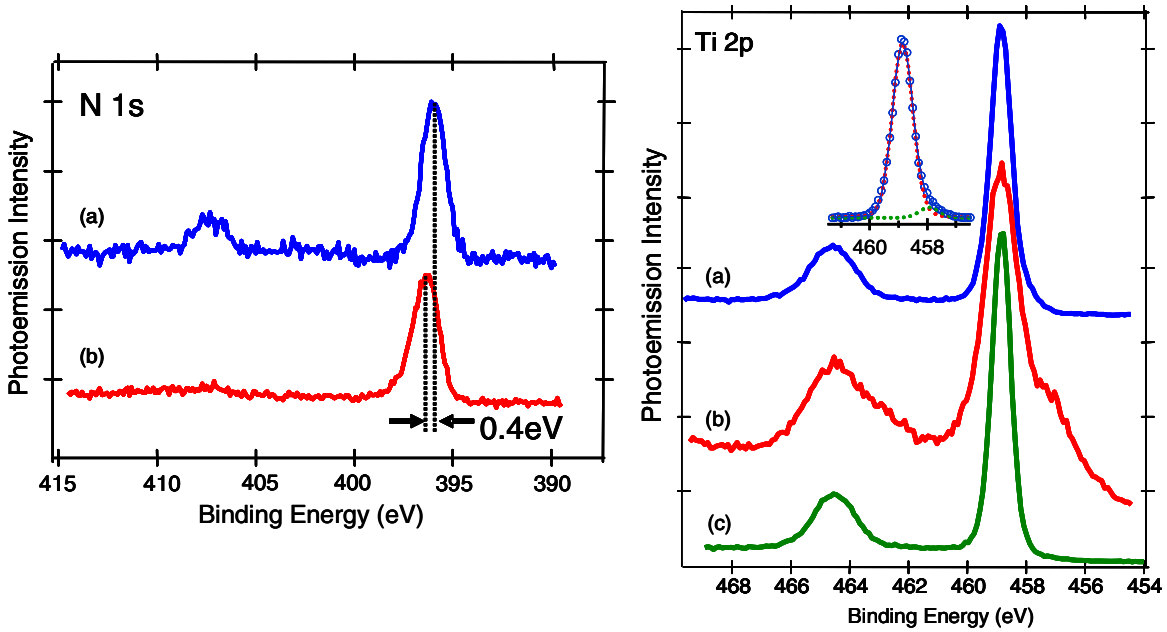

Figure 9. High-resolution core-level N 1s (left) and Ti 2p (right) XPS for $N_xTi_{1-x}O_2$ rutile films grown on rutile $TiO_2(110)$ grown under the same conditions as those described in the caption to figure 8.

accurate surface temperature determination for wide bandgap oxide substrates.

Acknowledgments

The author is indebted to his group members and colleagues at PNNL (Tim Droubay, Tiffany Kaspar, Irene Cheung, Yuanjie Li, and Takeo Ohsawa) for their patient and excellent work in the laboratory, and for many helpful discussions. The author also thanks Steven Heald and David Keavney of Argonne National Laboratory and Michael Toney of the Stanford Synchrotron Radiation Laboratory for their valuable contributions to this research. This work was performed in the Environmental Molecular Sciences Laboratory, a national scientific user facility sponsored by the Department of Energy's Office of Biological and Environmental Research and located at Pacific Northwest National Laboratory. This work was supported by the US Department of Energy, Office of Science, Division of Materials Science and Engineering, and Division of Chemical Sciences.

References

[1] McKee R A *et al* 1998 *Phys. Rev. Lett.* **81** 3014
[2] McKee R A *et al* 2001 *Science* **293** 468
[3] Haeni J H *et al* 2001 *Appl. Phys. Lett.* **78** 3292
[4] Schlom D G *et al* 2002 *MRS Bull.* **27** 198
[5] Lettieri J *et al* 2002 *J. Vac. Sci. Technol.* A **20** 1332
[6] Locquet J P *et al* 2006 *J. Appl. Phys.* **100** 051610
[7] Gustafsson T *et al* 2006 *Defects in High-k Gate Dielectric Stacks: Nano-Electronic Semiconductor Devices* (Berlin: Springer)
[8] Marchiori C *et al* 2006 *Appl. Phys. Lett.* **88** 072913
[9] Norga G J *et al* 2006 *J. Appl. Phys.* **99** 084102
[10] Locquet J P *et al* 1998 *Nature* **394** 453
[11] Bozovic I 2001 *IEEE Trans. Appl. Supercond.* **11** 2686
[12] Bozovic I *et al* 2001 *The Encyclopedia of Materials: Science and Technology* (Amsterdam: Pergamon)
[13] Schlom D G *et al* 2001 *The Encyclopedia of Materials: Science and Technology* (Amsterdam: Pergamon)
[14] Christiansen C *et al* 2002 *Phys. Rev. Lett.* **88** 037004
[15] Oh S *et al* 2005 *Appl. Phys. Lett.* **87** 213911
[16] Goldman A M 2006 *Appl. Surf. Sci.* **252** 3928
[17] Chambers S A *et al* 2002 *J. Magn. Magn. Mater.* **246** 124
[18] Schmehl A *et al* 2007 *Nat. Mater.* published online (September)
[19] Chambers S A *et al* 1999 *Surf. Sci.* **420** 111
[20] Chambers S A *et al* 1999 *Surf. Sci.* **420** 123
[21] Chambers S A *et al* 1999 *Surf. Sci.* **439** L785
[22] Chambers S A *et al* 2000 *Surf. Sci.* **450** L273
[23] Brown G E J *et al* 2001 *Nuclear Site Remediation: First Accomplishments of the Environmental Management Science Program* (Washington, DC: American Chemical Society)
[24] Bargar J R *et al* 2004 *Langmuir* **20** 1667
[25] Peden C H F *et al* 1999 *Catal. Today* **51** 513
[26] Altman E I *et al* 2002 *Thin Solid Films* **414** 205
[27] Chambers S A 2000 *Surf. Sci. Rep.* **39** 105
[28] Kaspar T C *et al* 2005 *Phys. Rev. Lett.* **95** 217203
[29] Kaspar T C *et al* 2006 *Phys. Rev.* B **73** 155327
[30] Chambers S A *et al* 2000 *Phys. Rev.* B **61** 13223
[31] Chambers S A *et al* 2007 *Chem. Phys.* **339** 27
[32] Cheung S H *et al* 2007 *Surf. Sci.* **601** 1754
[33] Osterwalder J *et al* 2005 *Thin Solid Films* **484** 289
[34] Dietl T *et al* 2000 *Science* **287** 1019
[35] Matsumoto Y *et al* 2001 *Science* **291** 854
[36] Chambers S A 2006 *Surf. Sci. Rep.* **61** 345
[37] Droubay T *et al* 2005 *J. Appl. Phys.* **97** 046103
[38] Coey J M D *et al* 2005 *Nat. Mater.* **4** 173
[39] Ye L-H *et al* 2006 *Phys. Rev.* B **73** 081304(R)
[40] Bryan J D *et al* 2004 *J. Am. Chem. Soc.* **126** 11640
[41] Bryan J D *et al* 2005 *J. Am. Chem. Soc.* **127** 15568
[42] Chambers S A *et al* 2003 *MRS Bull.* **28** 729
[43] Chambers S A *et al* 2003 *Phys. Rev.* B **67**
[44] Chambers S A *et al* 2003 *Appl. Phys. Lett.* **82** 1257
[45] Chambers S A *et al* 2005 *Thin Films and Heterostructures for Oxide Electronics* (New York: Springer)
[46] Chambers S A *et al* unpublished
[47] Butler W H *et al* 2003 *J. Appl. Phys.* **93** 7882
[48] Droubay T C *et al* 2007 *Phys. Rev.* B **75** 104412
[49] Asahi R *et al* 2001 *Science* **293** 269
[50] Wong M S *et al* 2006 *Thin Solid Films* **494** 244
[51] Okato T *et al* 2005 *Phys. Rev.* B **72** 115124
[52] Batzill M *et al* 2006 *Phys. Rev. Lett.* **96** 026103
[53] Matsui H *et al* 2005 *J. Appl. Phys.* **97** 123511
[54] Suda Y *et al* 2004 *Thin Solid Films* **453/454** 162
[55] Nakano Y *et al* 2005 *Appl. Phys. Lett.* **86** 132104
[56] Cheung S H *et al* 2007 *Surf. Sci.* at press